TID-4500, UC-35
Nuclear Explosions —
Peaceful Applications

LAWRENCE LIVERMORE LABORATORY
University of California/Livermore, California/94550

UCRL-51260

MECHANICAL PROPERTIES OF ROCKS FROM THE SITE OF THE RIO BLANCO GAS STIMULATION EXPERIMENT

R. N. Schock
H. C. Heard
D. R. Stephens

MS. date: August 30, 1972

Contents

MECHANICAL PROPERTIES OF ROCKS FROM THE SITE OF THE RIO BLANCO GAS STIMULATION EXPERIMENT

Abstract

The pressure-volume relationship, strength, differential stress-strain, and acoustic velocities were studied as a function of pressure for several samples of graywacke sandstone from the emplacement hole at the site of the Rio Blanco gas stimulation experiment. The results of these measurements are intended for use as input parameters in calculational codes which seek to predict the amount and extent of fracturing produced as a result of the detonation of an underground nuclear explosion. At laboratory strain rates ($\sim 10^{-5}$ sec^{-1}) the sandstones from the emplacement well are found to be rather compressible ($K \simeq 120$ kbar at overburden pressures) but have the relatively high shear modulus ($\mu \simeq 100$ kbar) characteristic of other similar graywacke sandstones. As with these other sandstones, the simulated plane shock-loading path shows pronounced departure away from the failure envelope. Some of this departure may be the result of strain-rate dependent processes. Failure in uniaxial compression is characterized by brittle fracture at mean pressures below 5 kbar and by macroscopic ductile flow above this pressure. Strength properties and the brittle to ductile transition are midway between those found for similar rock-types from the Gasbuggy and Wagon Wheel gas stimulation experiments.

Symbols and Units

σ	- principal stress denoted by subscript as maximum (1), intermediate (2) and minimum (3) stress or confining pressure (2=3)
ϵ	- strain denoted by subscript as radial (r), longitudinal (ℓ), or volume (V)
K	- bulk modulus (kbar)
μ	- shear modulus (kbar)
E	- Young's modulus (kbar)
ν	- Poisson's ratio
ρ	- density (g cm^{-3})
V_P, V_S	- compressional and shear velocity (km sec^{-1})
τ	- shear strength $(\sigma_1 - \sigma_3)/2$ (kbar)
P_m	- mean pressure $(\sigma_1 + \sigma_2 + \sigma_3)/3$ (kbar)
bar	- 10^6 dyne cm^{-2} = 10^{-3} kbar = 10^{-6} Mbar

× 3.8 cm). These samples were either compressed to failure at various confining pressures or evaluated in the indirect tensile (Brazil) tests at atmospheric pressure. Quasi-hydrostatic P-V data on similar cylindrical samples (1.3 cm diam × 2.5 cm) were obtained in a piston-cylinder device. A soft metal such as lead or tin was used as the pressure transmitting medium. Pressure-volume data were also obtained to 12 kbar using a hydrostatic pressure fluid to transmit pressure to the metal jacketed samples. Volumetric strains were monitored with foil strain gages cemented to the metal jacket. The jackets were initially seasoned to several tens of bars to shrink the jacket onto the rock sample.

Identically prepared specimens were used in the three-dimensional stress-strain experiments where axial load was applied with the piston of a piston-cylinder die in which the confining pressure could be externally controlled. The data from these three-dimensional experiments were then used to calculate deformation moduli over a wide range of stress states below and up to the failure envelope.

Acoustic velocities were obtained by measuring the transit time of a 1-MHz plane wave through jacketed samples.

Results and Discussion

PRESSURE-VOLUME CHARACTERISTICS

The P-V data for this sandstone are shown in Figs. 1 and 2 and summarized in Table 2. The results show considerable scatter. The data from hydrostatic tests indicate that the sandstone exhibits more compression than do the results from quasi-hydrostatic tests. Test results for the 5846 ft and 6442 ft samples appeared

Table 2. Pressure-volume characteristics of Rio Blanco sandstone.[a]

P (kbar)	V/V_o loading	V/V_o unloading	V (cm^3/g) loading	V (cm^3/g) unloading	K loading	P (kbar)	V/V_o loading	V/V_o unloading	V (cm^3/g) loading	V (cm^3/g) unloading	K loading
0	1.0000	0.9884	0.4014	0.3968	17.2	8.0	0.9556	0.9527	0.3836	0.3824	258.0
0.1	0.9942	-	0.3991	-	45.5	10.0	0.9483	0.9469	0.3806	0.3801	260.0
0.2	0.9920	-	0.3982	-	71.0	12.0	0.9417	0.9417	0.3778	0.3778	337.0
0.3	0.9906	-	0.3975	-	83.0	15.0	0.9340	0.9340	0.3749	0.3749	425.0
0.4	0.9894	-	0.3972	-	124.0	18.0	0.9274	0.9274	0.3723	0.3723	463.0
0.5	0.9886	0.9848	0.3969	0.3953	141.0	20.0	0.9234	0.9234	0.3707	0.3707	473.0
0.7	0.9872	-	0.3963	-	164.0	22.0	0.9195	0.9195	0.3691	0.3691	511.0
1.0	0.9854	0.9818	0.3955	0.3941	197.0	25.0	0.9141	0.9141	0.3670	0.3670	560.0
1.5	0.9829	-	0.3946	-	214.0	28.0	0.9092	0.9092	0.3650	0.3650	552.0
2.0	0.9806	0.9764	0.3937	0.3920	213.0	30.0	0.9059	0.9059	0.3637	0.3637	584.0
3.0	0.9760	0.9715	0.3918	0.3900	222.0	32.0	0.9028	0.9028	0.3624	0.3624	589.0
4.0	0.9716	0.9671	0.3900	0.3882	221.0	35.0	0.8982	0.8982	0.3606	0.3606	599.0
5.0	0.9672	0.9631	0.3883	0.3866	236.0	38.0	0.8937	0.8937	0.3588	0.3588	595.0
6.0	0.9631	0.9595	0.3866	0.3852	253.0	40.0	0.8907	0.8907	0.3576	0.3576	-
7.0	0.9593	0.9559	0.3851	0.3837	259.0						

[a] ρ_o = 2.491 g/cm^3; 50% saturated; 5862 ft and 6442 ft.

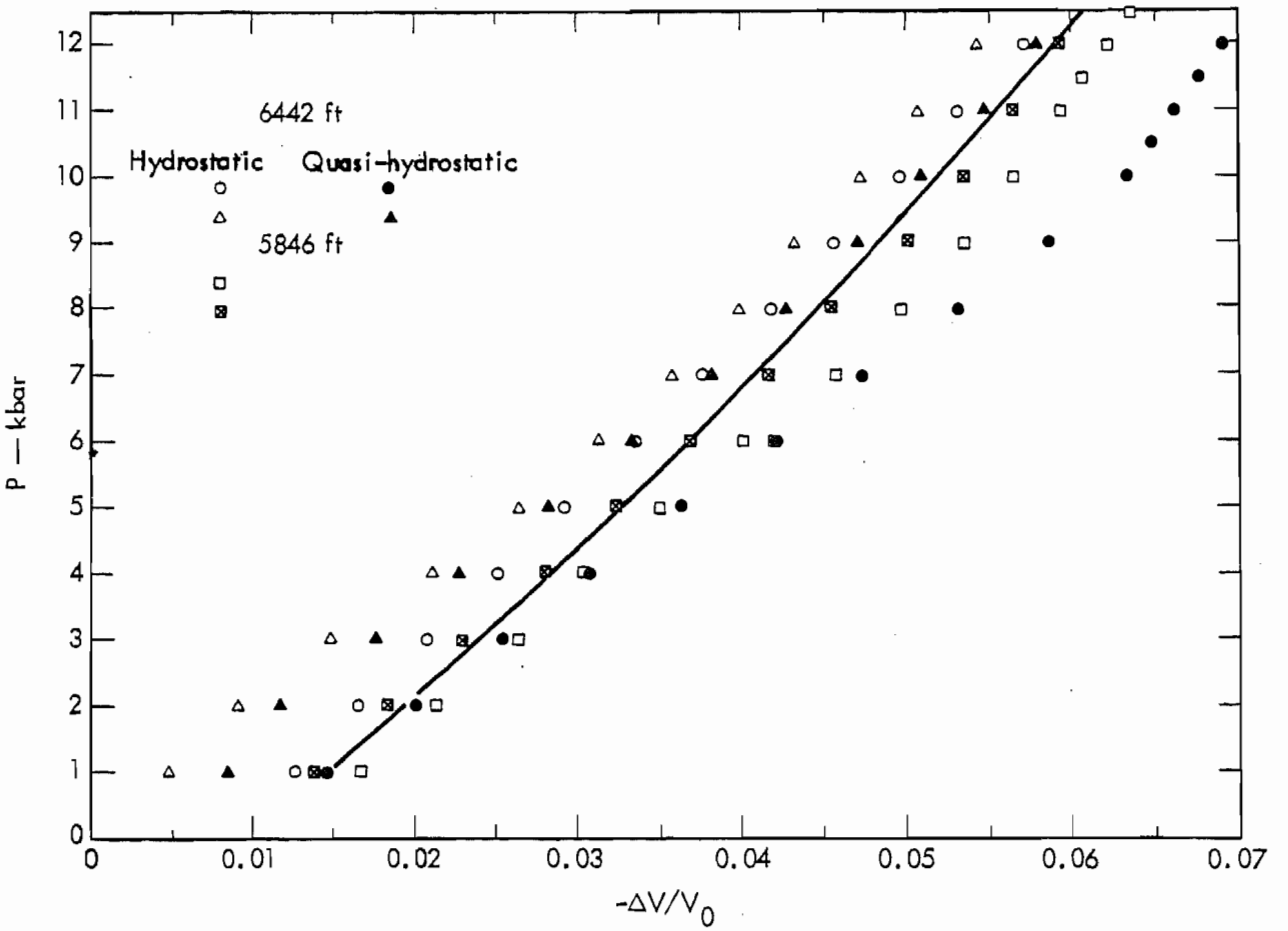

Fig. 2. Rio Blanco RB-E-01; pressure versus $\frac{\Delta V}{V_o}$ on loading. Curve is fit to hydrostatic data.

to be identical within the scatter of the data. There is less reproducibility in the Rio Blanco pressure-volume curve than in the curves of other sandstones previously examined,[4] suggesting a greater sample variability. These data also show inelastic effects. For example, the irreversible compaction upon unloading from 40 kbars is 1.1% as compared with the 3 to 4% initial gas-filled porosity.

Results for a sandstone from a well* 7.5 mi WSW of the Rio Blanco emplacement well are shown in Figs. 3 and 4 and in Table 3. This was the most porous of the samples studied (~18%). Both the hydrostatic and quasi-hydrostatic data show a distinct break in the P-V curve. This occurs at about 3 kbar and is undoubtedly related to the onset of pore collapse. Pore collapse seems to persist from 3 kbar to about 8 kbar where the P-V curve begins to stiffen again. Even so, the irreversible compaction from 40 kbar in this sample was only 3.4%, or 18% of the total porosity initially present in this sample. Inspection of the P-V data (Fig. 4) show that at about 4 kbar pressure there is only 6% difference in volume between the loading and unloading curves, and therefore considerable porosity was recovered upon unloading to 1 bar indicating

*Equity So. Sulfur Creek No. 4.

quasi-elastic recovery of some voids at low pressure.

It can be seen from the data presented in Table 3 that the bulk modulus at overburden pressure (≃440 bars) is 90 kbar, considerably lower than that found for the emplacement well samples.

UNIAXIAL STRESS MEASUREMENTS

Samples of graywacke from both depths in the Rio Blanco emplacement well were evaluated for compressive strength properties. These were the 5846 ft and 6442 ft materials. Tests were carried

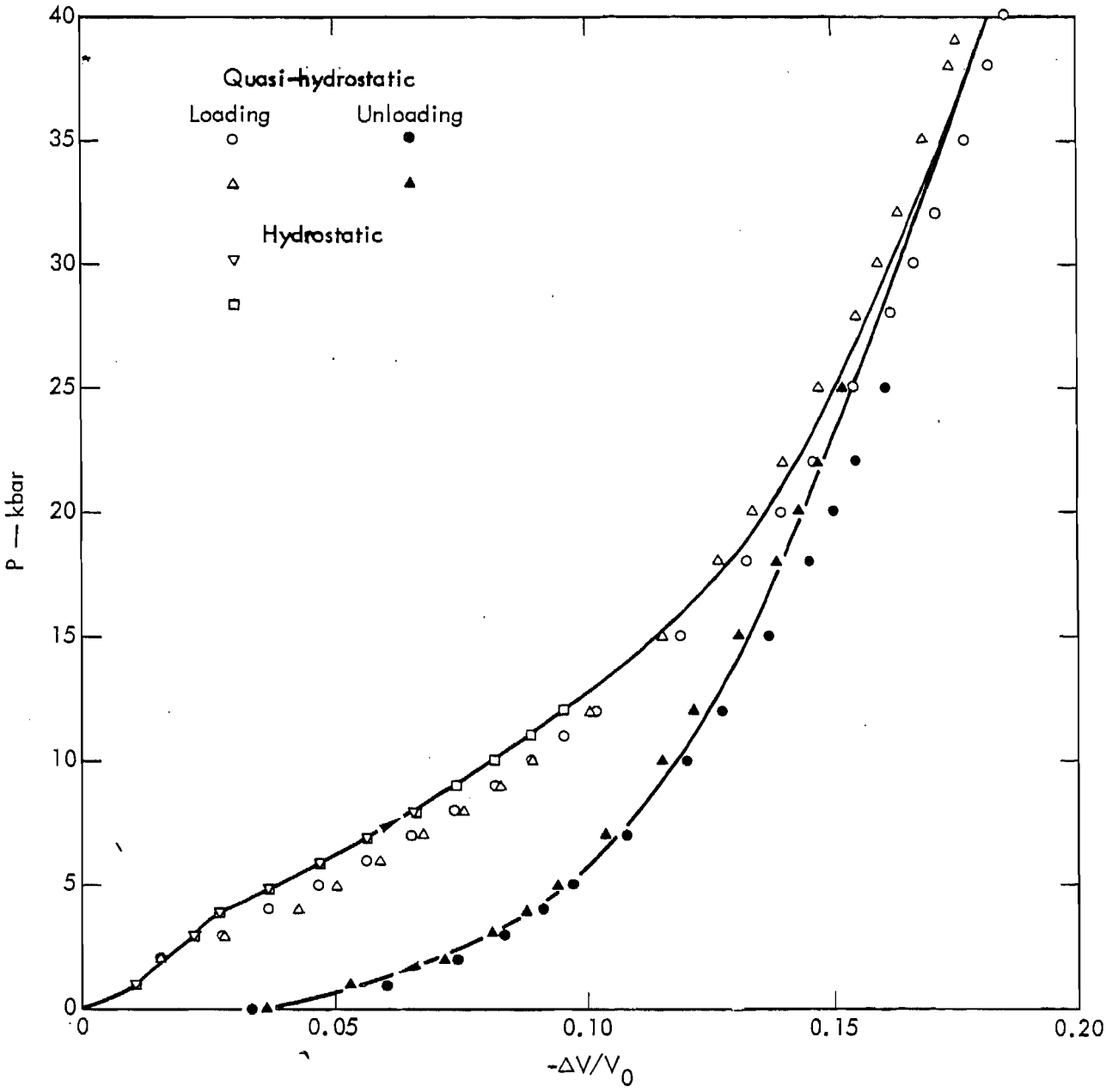

Fig. 4. S. Sulfur Creek No. 4; pressure versus $\Delta V/V_o$ on loading and unloading.

Table 5. Summary of uniaxial compression and Brazil test data for Rio Blanco 6442 ft sandstone (50% H_2O saturated).

Test type	Principal stress σ_1 (kbar)	Principal stress after fracture σ_1' (kbar)	Principal stress σ_2 (kbar)	Principal stress σ_3 (kbar)	Shear strength τ (kbar)	Shear strength after fracture τ' (kbar)	Mean pressure P_m (kbar)	Mean pressure after fracture P_m' (kbar)	Behavior
Brazil	0.138	0	0	-0.46	0.092	0	0.031	0	Brittle
Brazil	0.111	0	0	-0.37	0.074	0	0.025	0	Brittle
Uniaxial compression	0.70	0	0	0	0.35	0	0.23	0	Brittle
Uniaxial compression	0.78	0	0	0	0.39	0	0.26	0	Brittle
Uniaxial compression	0.67	0	0	0	0.34	0	0.22	0	Brittle
Uniaxial compression	0.72	0	0	0	0.36	0	0.24	0	Brittle
Uniaxial compression	0.92	0	0	0	0.46	0	0.31	0	Brittle
Uniaxial compression	4.81	3.91	1.00	1.00	1.91	1.45	2.26	1.97	Brittle
Uniaxial compression	7.44	6.37	2.00	2.00	2.72	2.19	3.82	3.46	Transitional
Uniaxial compression	10.06	-	3.00	3.00	3.53	-	5.36	-	Transitional
Uniaxial compression	13.37	-	4.00	4.00	4.69	-	7.13	-	Ductile
Uniaxial compression	16.15	-	5.00	5.00	5.58	-	8.72	-	Ductile
Uniaxial compression	17.87	-	6.00	6.00	5.94	-	9.97	-	Ductile

we are considering here, overall ductile behavior is due predominantly to the former mechanism with the individual brittle quartz and feldspar grains taking up the local displacements on a very fine scale.

Figures 5 and 6 illustrate the shear stress-mean pressure failure envelopes for the graywacke recovered from the depths noted above. The approximate transition from macroscopic brittle fracture to ductile flow occurs at approximately 5 kbar for the 5846-ft material (Fig. 5). This transition in material response is diffuse in the deeper graywacke, occurring over a mean pressure range of about 3.8 to about 5.4 kbar (Fig. 6). In the brittle region, large scale shear and extensile fractures predominate, with complete loss of cohesion of the test sample occurring only below about 2 kbar. Above the transition, little fracture or faulting is present (on the scale of the test sample); the stress-strain curves show moderate to strong work hardening with the strain being more or less homogeneously distributed throughout the sample (at least on the scale of a few tens of microns).[12] The limiting strength after fracture with consequent loss of cohesion is also shown (dashed curve) in both figures. Note that the level of shear stress supported by this sandstone after fracture is only slightly less than that of the coherent material.

The failure envelopes for both graywackes are virtually identical; the 6442-ft

material is only slightly weaker at all except the lowest pressures. Both envelopes are nearly linear (except at the lowest pressures) with an average slope of 0.56.

Tensile strengths for both graywacke samples range from 33 to 46 bars, averaging about 39 bars. The 6442-ft material seems slightly, but not significantly, stronger in tension. No tensile results are available at pressure, but based on similar measurements on three other rock types,[13] the tensile strength is expected to remain independent of confining pressure.

In addition, both uniaxial compression and Brazil data have also been determined on the graywacke from the S. Sulfur Creek well. This material was tested dry. The failure envelope illustrated in Fig. 7 for this graywacke is based on differential stress-axial strain data and ductility criteria as discussed above. All results for this material are summarized in Table 6.

Comparison between Fig. 7 and Figs. 5 and 6 shows the shear strength of the Sulfur Creek material in the 4 to 10 kbar range to be only about 60% of that of the sandstones from the emplacement well. The envelope is curved to the highest pressures but in the intermediate range, the slope is approximately 0.36, much lower than for the two emplacement hole materials. The brittle-ductile transition is also lower; 2.9 kbar compared to 3.8 to 5.4 kbar. However, the tensile strength is almost identical (Table 6). This different behavior pattern, characteristic of the Sulfur Creek sandstone, is not thought to be due to the initial differences in water saturation. Support for this contention can be found in the nearly identical results for a dry and a 50% saturated graywacke from Wyoming.[4] The apparent increased ductility and lower strength of

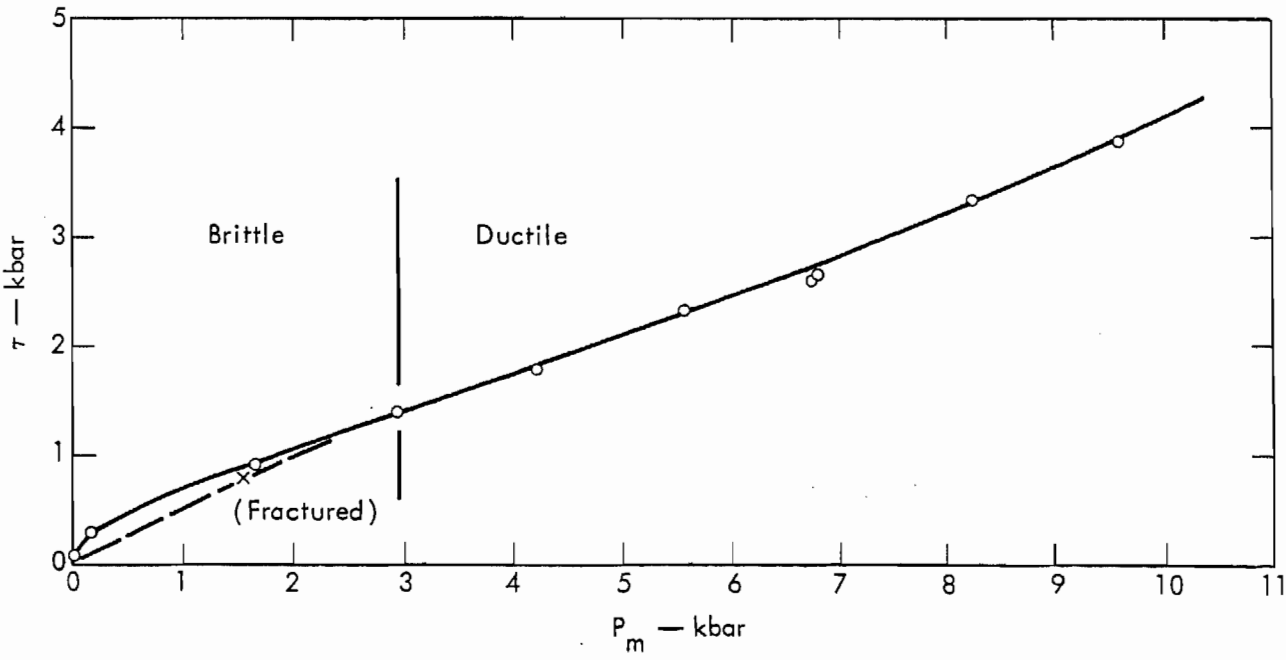

Fig. 7. S. Sulfur Creek No. 4 dry: shear stress-mean pressure failure envelope.

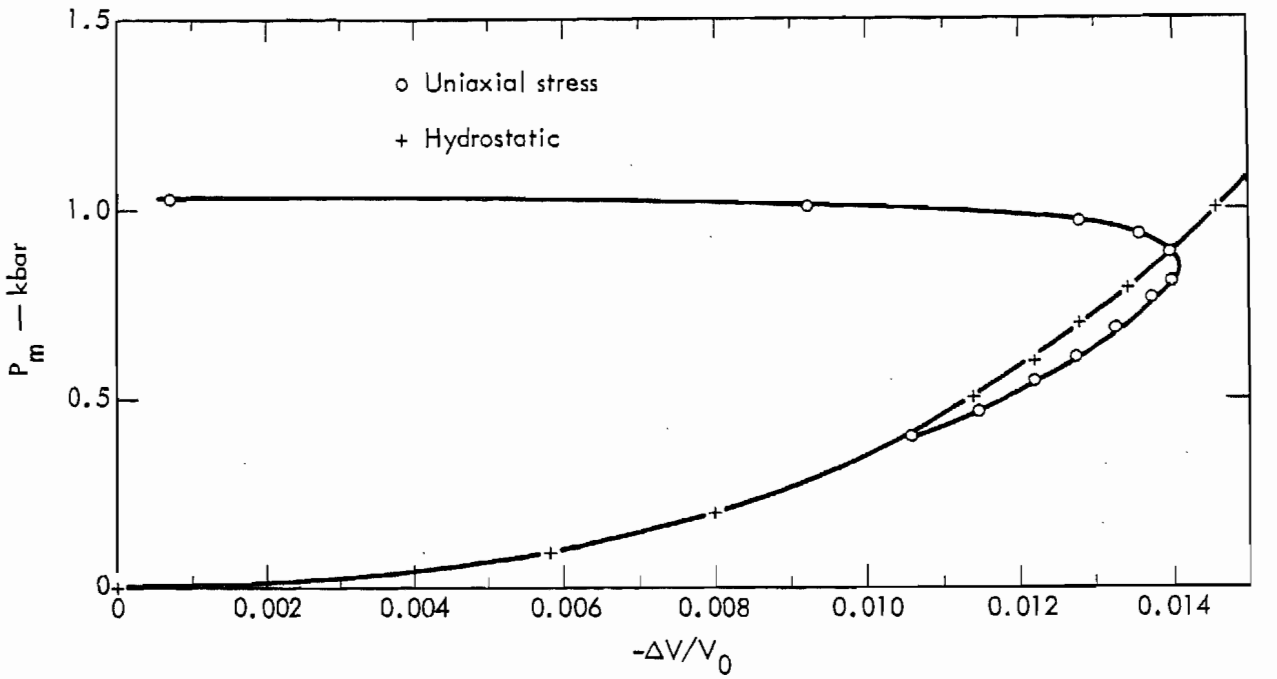

Fig. 8. Rio Blanco RB-E-01 5846 ft: mean pressure versus $\Delta V/V_0$ under conditions of uniaxial stress (σ_3 = 400 bars) and hydrostatic loading.

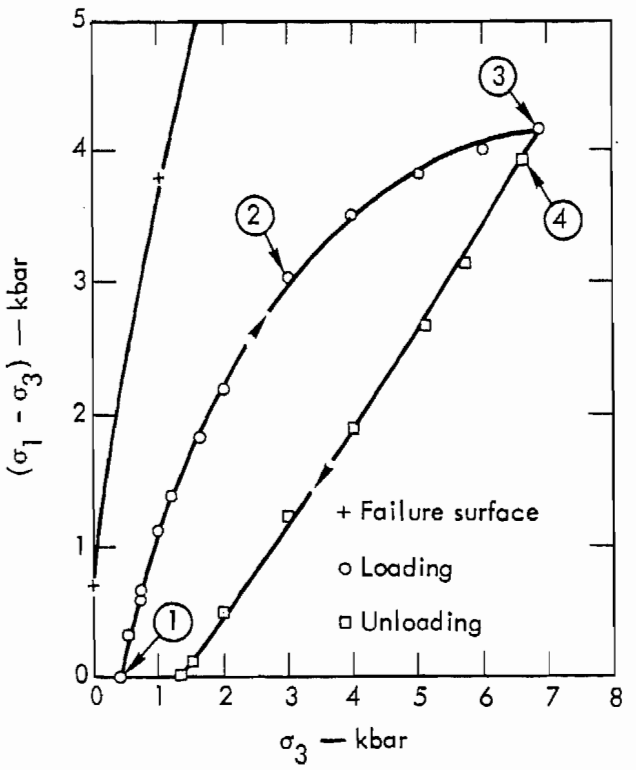

Fig. 9. Rio Blanco RB-E-01 6442 ft: axial differential stress ($\sigma_1 - \sigma_3$) versus confining pressure for loading and unloading under conditions of uniaxial strain ($d\epsilon_r = 0$). The failure envelope from Fig. 6 is shown for comparison. Numbered points referred to in text.

ductile nature of the Rio Blanco material as evidenced by the lower observed brittle-ductile transition pressure.

UNIAXIAL STRAIN MEASUREMENTS

Loading data under conditions of uniaxial strain ($d\epsilon_r = 0$) were taken on samples from both depths in the emplacement well. Within experimental error, the results were identical. Typical results in shear stress-confining pressure space are shown in Fig. 9 for a 6442 ft sample loaded from 400 bars (approximate overburden pressure). The corresponding strain data are shown in Fig. 10. As was observed for the Wagon Wheel sandstone, the loading path is apparently diverging away from the failure surface at the higher mean pressures. The steep initial slope in Fig. 8 is a reflection of the high shear modulus to bulk modulus ratio (low Poisson's ratio) characteristic

another resulting in a decreasing shear modulus. The deformation may be idealized as a small initial elastic region followed by increasing inelastic compaction. Upon the initial release of axial stress from the highest value attained, the deformation is again predominantly elastic as evidenced by a large increase in the shear modulus. Thus the initial effective moduli (point 1, Fig. 9) are K = 118 kbar (in good agreement with Fig. 1), μ = 99 kbar and assuming elasticity, ν = 0.17. At 3 kbar axial stress difference (point 2) K has increased to 182 kbar, μ has decreased to 62 kbar, and ν = 0.35. By 4.2 kbar axial stress difference (point 3) the effective moduli are K = 360 kbar, μ = 40 kbar and ν = 0.45. Upon release of the applied axial stress (point 4), the effective μ increases drastically to 125 kbar, K has remained at 360 kbar and the effective ν is 0.34.

There are two phenomena (perhaps interrelated) which may serve to facilitate fracture during a dynamic loading event such as a nuclear explosion. The first is the tendency toward brittle fracture at higher mean pressures with higher strain rates. The second is that the processes responsible for the increasing amount of curvature of the uniaxial strain loading curve (associated with large deformations) at high axial stress differences presumably involve intergranular movement and are therefore inherently time dependent. In a purely elastic solid, loading would take place according to the elastic moduli. If this sandstone were considered to be elastic except for time-dependent processes, loading would be linear and to failure along a slope defined by the initial loading moduli (approximately point 1, Fig. 9). In reality, neither the path shown in Fig. 9 nor the pure elastic path will be the actual shock-loading path, but rather these probably define limits to the shock path. Good agreement has been found between the shock loading states (axial stress and strain) and those obtained in uniaxial strain experiments for the Wagon Wheel sandstone.[15] However, since the tangential stress (σ_3) is not determined in shock-wave experiments, it is impossible to determine the shock loading path with respect to the failure surface in Fig. 9.

The axial stress-strain data shown in Fig. 10 indicate a slight break in the loading path about 3 kbar σ_1. This is similar to an observed break in both the Wagon Wheel (Fig. 11) and Gasbuggy[9] sandstones. However, unlike both of these rocks, there appears to be no <u>significant</u> loading below the hydrostat beyond this break. This is probably due to the initial high compressibility of the Rio Blanco samples. Thus, the shear stress can accomplish little enhanced compaction at higher mean pressures because porosity has already been lost at low pressure. As previously noted, there is some observed loading below the hydrostat in uniaxial stress experiments where the shear stress-mean pressure ratio increases much more rapidly.

After loading to 11 kbar in uniaxial strain (σ_1), permanent compaction is observed. Upon removal of the stress difference, 0.3% permanent compaction results (Fig. 10) as compared with the 1.1% on unloading from 40 kbar hydrostatic pressure (Fig. 1).

Since the traveltime of an acoustic wave is very sensitive to its mean free path, the moduli derived from acoustic velocities are very sensitive to any deformation mechanism which alters that path. Movement along a surface across which a wave is propagating is not likely to affect the wave velocity as markedly as the initial fracturing (formation) of that surface. It is quite possible, therefore, that the fracturing of cement between grains affects the wave propagation significantly while the fracture itself does not cause any significant volume compression. At higher pressures, as grains begin to move relative to one another, volume compression becomes pronounced. However the resulting lower porosities now result in a more efficient path for wave propagation and a consequent increase in velocity and derived K. At still higher pressures, well beyond the extent of the data in Fig. 12, the moduli would converge as pores and cracks are squeezed shut and the rock begins to approach a theoretically dense elastic solid.

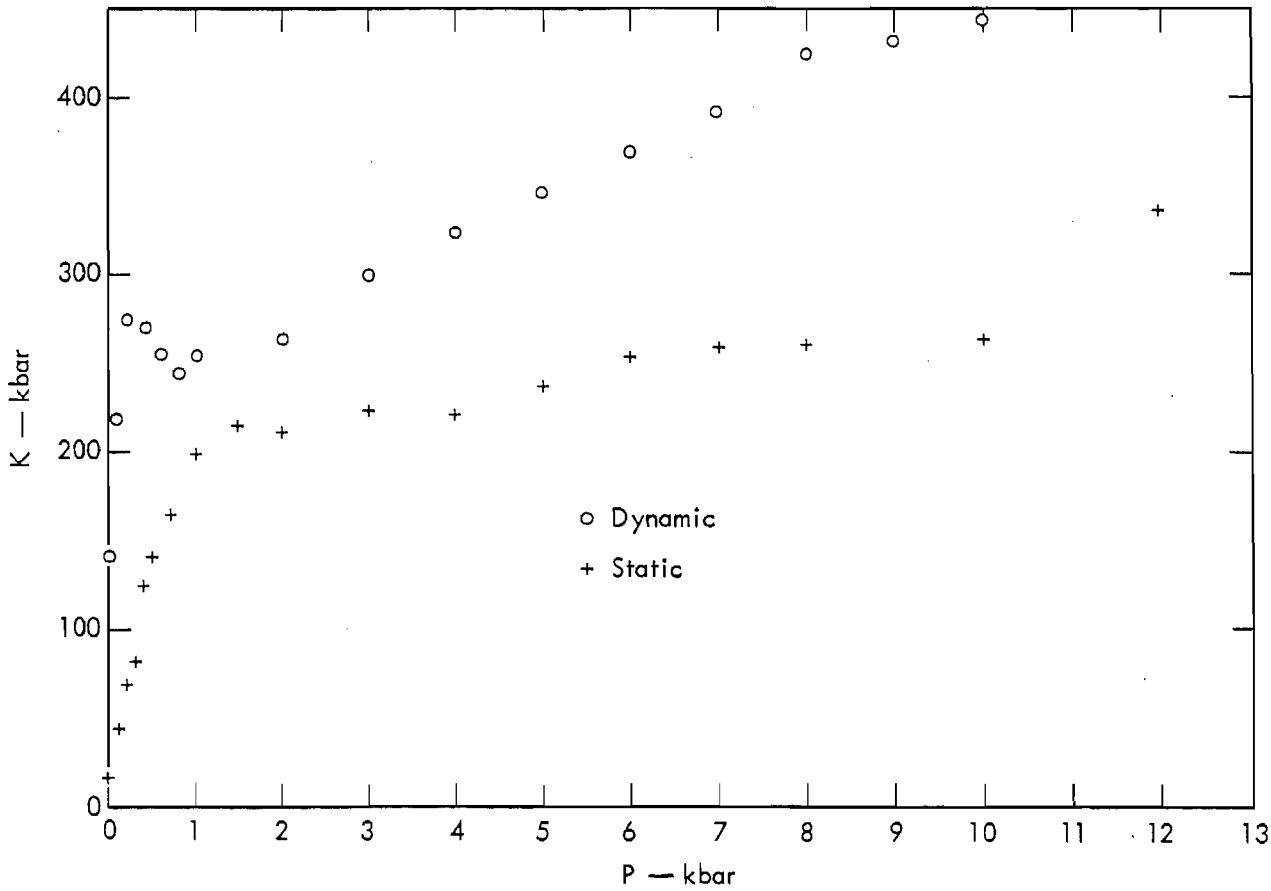

Fig. 12. Rio Blanco RB-E-01 6442 ft: static and dynamic bulk moduli as a function of hydrostatic pressure.

Appendix: Acoustic Compressional and Shear Velocities

The data presented in Table A-1 represent velocities calculated from travel-times of both compressional and shear waves propagating normal to the bedding and the moduli derived therefrom with the assumption of elasticity. Densities are determined by continually integrating the computed bulk modulus. The sandstone was initially 50% water-saturated at 1 atm.

Table A-1. Compressional and shear velocity and derived elastic moduli, Rio Blanco RB-E-01, 6442 ft.

Pressure (kbar)	ρ (g/cc)	V_P (km/sec)	V_S (km/sec)	K (Mbar)	μ (Mbar)	ν	E (Mbar)
0	2.47	3.40	2.12	0.138	0.111	0.18	0.262
0.10	2.48	4.02	2.34	0.229	0.135	0.25	0.333
0.20	2.48	4.50	2.63	0.274	0.171	0.24	0.424
0.40	2.48	4.70	2.90	0.270	0.209	0.19	0.498
0.60	2.48	4.79	3.08	0.254	0.235	0.15	0.540
0.80	2.48	4.83	3.18	0.245	0.251	0.12	0.561
1.00	2.48	4.88	3.18	0.255	0.252	0.13	0.568
2.00	2.49	4.99	3.27	0.265	0.267	0.12	0.599
3.00	2.50	5.14	3.28	0.301	0.270	0.16	0.623
4.00	2.51	5.24	3.30	0.325	0.274	0.17	0.641
5.00	2.52	5.33	3.31	0.346	0.276	0.19	0.655
6.00	2.53	5.40	3.32	0.367	0.278	0.19	0.666
7.00	2.53	5.50	3.32	0.393	0.279	0.21	0.677
8.00	2.54	5.60	3.32	0.424	0.280	0.23	0.689
9.00	2.55	5.64	3.32	0.434	0.281	0.23	0.694
10.00	2.55	5.67	3.33	0.444	0.283	0.24	0.700

External Distribution

C. McFarland
J. Lewis
Defense Nuclear Agency
Washington, D. C.

B. Brown
W. Davis
B. Grote
Defense Atomic Support Agency
Albuquerque, New Mexico

J. M. Logan
Texas A & M University
College Station, Texas

R. A. Black
S. Ruby
D. C. Russell
J. Pearce
Dept. of Defense
Washington, D. C.

J. Trulio
Applied Theory, Inc.
Los Angeles, California

B. M. Butcher
L. M. Lee
Sandia Laboratories
Albuquerque, New Mexico

J. McQueen
R. McQueen
Los Alamos Scientific Laboratory
Los Alamos, New Mexico

F. Sauer
C. Godfrey
Physics International Company
San Leandro, California

H. L. Brode
The Rand Corporation
Santa Monica, California

D. E. Willis
University of Michigan
Ann Arbor, Michigan

P. N. LaMori
Battelle Memorial Institute
Columbus, Ohio

J. E. Whitener
H. Cooper
R & D Associates
Santa Monica, California

P. Hoekstra
E. Chamberlain
U. S. Army Terrestrial Sciences Center
Hanover, New Hampshire

P. Randolph
L. Rogers
El Paso Natural Gas Company
El Paso, Texas

M. Baron
I. Nelson
Paul Weidlinger Consulting Engineer
New York, New York

J. Isenberg
Agbabian-Jacobsen Associates
Los Angeles, California

D. Grine
J. T. Cherry
D. Rinney
System, Science and Software
La Jolla, California

S. Green
Terra Tak
Salt Lake City, Utah

J. B. Walsh
W. Brace
Massachusetts Institute of Technology
Cambridge, Massachusetts

J. C. Jamieson
University of Chicago
Chicago, Illinois

S. Katz
Rensselaer Polytechnic Institute
Troy, New York

T. Ahrens
California Institute of Technology
Pasadena, California

V. K. Gregson
General Motors Corporation
Warren, Michigan

M. Rosenblatt
Shock Hydrodynamics, Inc.
Sherman Oaks, California

E. D. Peixotto
J. Zelasko
U. S. Waterways Experiment Station
Vicksburg, Mississippi

R. H. Gates
Explosive Excavation Research Office
Livermore, California

Chi-Yuen Wang
University of California
Berkeley, California